UC Berkeley

Title

Compton and Proximity Imaging of Ac In Vivo With a CZT Gamma Camera: A Proof of Principle With Simulations

Permalink

https://escholarship.org/uc/item/0205393t

Journal

ISSN

Authors

Caravaca, Javier
Huh, Yoonsuk
Gullberg, Grant T
et al.

Publication Date

2022-11-01

DOI

Peer reviewed

Compton and proximity imaging of ^{225}Ac in vivo with a CZT gamma camera: a proof of principle with simulations

Javier Caravaca,

Yoonsuk Huh,

Grant T. Gullberg,

Youngho Seo

Department of Radiology and Biomedical Imaging of the University of California San Francisco in San Francisco (CA) USA.

Abstract

In vivo imaging of ^{225}Ac is a major challenge in the development of targeted alpha therapy radiopharmaceuticals due to the extremely low injected doses. In this paper, we present the design of a multi-modality gamma camera that integrates both proximity and Compton imaging in order to achieve the demanding sensitivities required to image ^{225}Ac with good image quality. We consider a dual-head camera, each of the heads consisting of two planar cadmium zinc telluride detectors acting as scatterer and absorber for Compton imaging, and with the scatterer practically in contact with the subject to allow for proximity imaging. We optimize the detector's design and characterize the detector's performance using Monte Carlo simulations. We show that Compton imaging can resolve features of up to 1.5 mm for hot rod phantoms with an activity of 1 μCi, and can reconstruct 3D images of a mouse injected with 0.5 μCi after a 15 minutes exposure and with a single bed position, for both ^{221}Fr and ^{213}Bi. Proximity imaging is able to resolve two 1 mm-radius sources of less than 0.1 μCi separated by 1 cm and at 1 mm from the detector, as well as it can provide planar images of ^{221}Fr and ^{213}Bi biodistributions of the mouse phantom in 5 minutes.

Index Terms—

preclinical imaging; targeted alpha therapy; actinium-225; Compton imaging; proximity imaging

I. Introduction

Targeted alpha therapy (TAT) has shown excellent results in the treatment of different types of solid and liquid cancers, with superior performance than the standard beta radiotherapy with 177Lu in certain scenarios [1, 2]. The higher linear energy transfer of alpha particles over beta particles offer a much more targeted modality. Alpha particles deposit all their

This work did not involve human subjects or animals in its research.

energy in a range of the order of microns, as opposed to beta particles, whose millimeters range leads to a higher healthy tissue damage [3].

^{225}Ac is a very promising alpha emitter for TAT [4–6] due to their high delivered dose (four alpha particles emitted in its decay chain) and its half-life of 9.9 days, which makes radiopharmaceutical handling and patient delivery easier. A crucial step in the development of novel ^{225}Ac TAT radiopharmaceuticals is the characterization of their pharmacokinetics (PK), typically done determining its efficacy and toxicity over time in small animals (usually mice or rats) [7]. This is particularly important in ^{225}Ac since it decays to four other alpha emitters (^{221}Fr, ^{217}At, ^{213}Bi and ^{213}Po) and the recoil and different chemical affinity can detach them from the radiopharmaceuticals, releasing a toxic dose in healthy tissue [8–10].

PK studies are typically done ex vivo by sacrificing a large number of mice at different time points, dissecting their organs, and deploying them in a gamma or alpha counter to obtain the per-organ dose as a function of time [11, 12]. In vivo methods are preferred since they are easier to execute compared to the ex vivo approach, they provide a 3D dose maps, and they would enable the study of PK in the same mouse over the treatment and evolution of the malignancy.

Since alpha particles are absorbed in the tissue, the only externally detectable signals from ^{225}Ac are gamma-rays and beta particles. Beta particles rarely exit the body, but they can produce Cherenkov light in tissue that has been demonstrated as an imaging tool (Cherenkov Luminescence Imaging or CLI), although it presents some limitations, namely, it cannot provide specific information of the location of each alpha emitter in the ^{225}Ac decay chain, dosimetry studies are subject of important uncertainties, and it is unable to identify the type of radionuclide [13].

The dominant gamma ray emissions of ^{221}Fr (218 keV) and ^{213}Bi (440 keV), with branching ratios 11.4% and 25.9% respectively, can be used to obtain quantitative dose maps using single photon emission computed tomography (SPECT) [14]. This has been demonstrated with a commercial preclinical micro-SPECT/CT (Vector [15]) with phantoms that required doses two orders of magnitude higher than the toxicity limit in mice [16] and with 24-hours exposures. These features prohibit in vivo imaging. In clinical trials, commercial SPECT/CT systems have shown promise detecting ^{225}Ac in post-therapy whole-body imaging for tracer localization and dosimetry in cases of metastatic cancer (mainly in castration-resistant prostate cancer) [17–21]. However, the obtained tumor uptake images and dose maps suffer from low count statistics and a very poor signal-to-noise ratio compared to the images from ^{18}F and ^{68}Ga positron emission tomography and ^{177}Lu SPECT/CT. This makes lesion delineation extremely hard and it results in an imprecise dosimetry.

Gamma ray imaging of ^{225}Ac daughters is extremely challenging due to the very low dose injected and the relatively high energy of the emitted gamma rays. In preclinical settings, a typical ^{225}Ac dose in mice with prostate cancer tumor models is ~1 MBq/kg [22], which is more than two orders of magnitude lower than those used for ^{177}Lu beta therapy (~500 MBq/kg) [22]. Regarding the energy of the emitted gamma rays, it is too high (>200 keV) to be detected with a good efficiency by current SPECT systems, given that they

are typically optimized for the 140 keV gamma emission of ^{99m}Tc. A novel multi-pinhole detector is proposed in [23] that yields a high sensitivity and good energy resolution for a broad range of energies 100 keV-500 keV. Despite the progress, in vivo imaging of ^{225}Ac radiopharmaceuticals has not been demonstrated yet.

The goal of this paper is to propose a new system that can image the ^{225}Ac gamma-ray emissions independently in TAT radiopharmaceuticals injected in mice in order to enable in vivo dosimetry. Given that the main driver of the low sensitivity is the collimator present in standard SPECT systems, we propose an alternative collimator-less approach that combines Compton imaging with proximity imaging. Compton imaging is a modality that has successfully demonstrated imaging of radionuclides in vivo in different scenarios: ^{99m}Tc imaging [24, 25], other single tracers imaging [26], multi-tracer preclinical [27–30], and clinical imaging [31]. Simulations predict that Compton imaging provides a higher gamma ray detection efficiency and performs better than standard SPECT systems with collimators at energies over 300 keV [32, 33], since, at higher energies, Compton scattering dominates over photo-electric absorption (PA) and its angular resolution improves. Proximity imaging provides an extremely high sensitivity that can be used to image extremely low dose activities with exposures of a few minutes, as demonstrated in [34, 35] for low energy sources. We explore a cadmium-zinc-telluride (CZT) gamma camera that uses both modalities in order to enable a high sensitivity system, able to reconstruct in vivo images of ^{221}Fr and ^{213}Bi from ^{225}Ac radiopharmaceuticals. In [36], a GAGG Compton camera is proposed to image ^{225}Ac, showing promising results with simulated phantoms, although with doses that are much higher than the safe dose.

In this paper, we present the performance predicted by Monte Carlo (MC) simulations of a CZT gamma camera that enables Compton and proximity imaging, using a mouse phantom ^{225}Ac under realistic dose conditions. The camera design and MC model are discussed in Sec. II, the Compton and proximity reconstruction algorithms are presented in Sec. III, the detector and reconstruction optimization and performance are shown in Sec. IV, the results with hot rod phantoms and a mouse phantom are in Sec. V, an extensive discussion about the relevance and limitations of this study is given in Sec. VI, and Sec. VII concludes.

II. Gamma camera design

We have designed a multi-modality system that enables Compton and proximity imaging at the same time, whose basic design consists of two detector heads set in parallel, where each detector head is made of two CZT parallel planes (Fig. 1). The principle of Compton imaging requires the detection of a Compton scattering followed by a PA. This is enabled in our system by using a scatterer, intended to provide the Compton scattering, and an absorber at the downstream position, intended to provide the PA. By using a high-Z scatterer, we also enable a high rate of PAs in a detector in contact with the subject (Fig. 1), which is used by our proximity reconstruction. There is also a non-negligible rate of Compton back-scatters that provides a Compton interaction in the absorber and a PA in the scatterer. Despite this, we will keep using the scatterer-absorber nomenclature through this paper for simplicity.

A. Monte Carlo model

A detector model is implemented using the GEANT4-based [38] open software RAT-PAC [39]. The Livermore Physics list is used to model the gamma ray interactions and the electron propagation through the materials. The CZT material is defined as Cd(0.9)Zn(0.1)Te, with mass proportions 0.43:0.03:0.54 (Cd:Zn:Te) and a density of 5.8 g/cm^3. We consider four detector planes with the same size of 100 mm × 100 mm with a separation between scatterers of 31 mm, which is the minimum distance that can fit the mouse phantom in an horizontal position. The CZT thickness, pixel size, and distance between scatterer and absorber are optimized in Sec. IV–A. The MOBY 2.0 mouse phantom [37] is imported in GEANT4 using a voxelized model with 196 × 186 × 745 voxels of (0.145 mm)^3 and 15 organs (lungs, muscle, intestine, bone marrow, pancreas, brain, heart, kidney, blood, liver, spleen, spine, skull, cortical, rib). The hot rod phantoms are simulated as a cylindrical piece of acrylic with water-filled rods and their geometry are specified in Sec. V.

Our detector response model includes the position and energy resolution as a Gaussian smearing implemented after the Geant4 simulations. When a gamma ray interaction (Compton or PA) occurs in any detector plane, the centroid of the energy deposition and the amount of deposited energy are recorded for each pixel. The center of the pixel is used as the landscape (XZ) position of the interaction, while the Y (transversal) position is provided by the true Y location of the center of the energy cluster smeared by a Gaussian in order to model the depth of interaction (DOI) of the CZT detectors. Our nominal DOI in our model is 1 mm full width half maximum (FWHM) and the dependence of the imaging performance with DOI is discussed in Sec. IV-A4. The Compton imaging quality heavily depends on the energy resolution. We consider a Gaussian energy resolution model, whose width depends on the square root of the detected energy E, given the Poisson nature of the CZT charge collection

$$\Delta E = 0.065\sqrt{122} \times \sqrt{E} \tag{1}$$

The constant is defined such that the resolution at 122 keV is 6.5% FWHM. Imaging performance as a function of the energy resolution is discussed in Sec. IV-A5. Timing resolution is not considered in this study since its effect is assumed to be second-order given the relatively low count rate associated with the low injected activities. The CZT detection efficiency is not modeled and it is assumed to be 100% (see Sec. VI). Individual gamma rays of energies corresponding to ^{221}Fr and ^{213}Bi decays are simulated using a particle gun generator. Each MC event corresponds to a single gamma ray, so no pile up is considered in this study, since for extremely low activity sources it is a negligible effect. Contamination of ^{213}Bi events in the ^{221}Fr energy window is estimated to be 7.6 ± 0.2% for a simulated source at the center of the detector. Given this component is small, we do not simulate it in the ^{221}Fr imaging analysis. A summary of the modeled values is in Table I, which are further justified in Sec. IV.

III. Image reconstruction

Two independent image reconstruction algorithms have been implemented, one for each modality. We consider a GPU-accelerated list-mode ordered subset expectation maximization (LM-OSEM) for Compton imaging and a standard ordered subset expectation maximization (OSEM) for proximity. The combination of both modalities into a single algorithm with potentially better performance is out of the scope of this paper and it will be explored in the future.

A. Compton imaging—The Compton scattering angle θ_c of a gamma ray of energy E_γ is determined by the energy of the knocked-out electron, which corresponds to the energy deposited by the Compton electron, E_C, by the expression

$$\cos\theta_c = 1 - \frac{m_e c^2 E_C}{E_\gamma (E_\gamma - E_C)},\tag{2}$$

where m_e is the rest mass of the electron and c is the speed of light in vacuum. Uncertainties in this angle come from the detector energy resolution and from the unknown energy of the electron in the atom before the interaction (Doppler broadening [40–42]). Thus, given the position of the Compton interaction $\overrightarrow{r}_C$ and the position of the PA $\overrightarrow{r}_{PA}$, the original direction of the incoming gamma ray can be constrained to a conical surface (Fig. 2).

The identification of which location corresponds to the Compton interaction and which one corresponds to the PA is not trivial. We assume that the Compton interaction occurs in the scatterer and that the PA occurs in the absorber, which partially degrades image quality due to the back-scattering events.

The sensitivity to coincidence events could be improved by including events with multiple Compton interaction by selecting events with more than one pixel hit in each detector. The ratio of multi-Compton over single-Compton events without requiring a fixed number of pixels are (29.8 ± 0.5) % for ^{213}Bi and (14.4 ± 0.3) % for ^{221}Fr. Including these events would increase the sensitivity accordingly. However, given their more complicated topology than single-Compton events, their integration in the image reconstruction is not trivial and the impact in image quality needs to be evaluated. In this paper we only explore single Compton interaction events and we leave this refinement for future analyses.

1) Compton coincidence event selection: For a known E_γ, the reconstruction of the Compton kinematics is reduced to determining E_C, $\overrightarrow{r}_C$ and $\overrightarrow{r}_{PA}$. For this purpose, we select events that present energy deposited in a single pixel of the scatterer and energy deposited in a single pixel of the absorber. The sum of these two energies is required to be larger than 430 keV for ^{213}Bi imaging and to be between 210 keV and 230 keV for ^{221}Fr. The rate of back-scatter events after this selection is 21% for ^{213}Bi and 11% for ^{221}Fr.

2) GPU-accelerated LM-OSEM for Compton imaging: LM-OSEM [43, 44] is a popular reconstruction algorithm used in SPECT that has been previously applied to Compton imaging with good results [29, 31, 32]. The number of selected Compton

coincidence events N^C are randomly sorted in S subsets with approximately the same number N_s^C of events each. The activity λ_j in voxel j is given by the iterative expression

$$\lambda_j^{k+1} = \frac{\lambda^k}{\varepsilon_j} \sum_{N_s^C} \frac{A_j(E_C, \theta)}{\sum_l A_l(E_C, \theta)\lambda_l^k},$$

(3)

where λ_j^{k+1} is the activity in voxel j for iteration step $k+1$, λ_j^k is the activity in the same voxel in the previous iteration step, ε_j is the Compton sensitivity, defined as the probability of detecting a Compton coincidence event from a gamma ray generated in voxel j, N_s^C is the number of events in subset s, and A_j is the Compton system matrix, defined as the probability of detecting a gamma ray generated in voxel j with an energy deposited in scatterer E_C and at an angle θ between the voxel direction $\vec{r}_{j,C}$ and the scattered gamma direction $\vec{r}_{PA,C}$ (Fig. 2). This equation is applied to the subsequent subsets by updating λ_j^k with the result of the previous subset. One OSEM iteration corresponds to the application of Eqn. (3) to every subset in succession. A voxelized volume is defined with voxel centers $\vec{r}_j$, and voxel size optimized depending on the imaged subject (Sec. IV-B1).

The problem is now reduced to computing A_j and ε_j, which we achieve via MC simulations. Four billions single gamma ray events are generated at the center of the detector using our MC model, which takes about 400 CPU hours. The event selection (Sec. III-A1) is applied and $A_j(E_C, \theta)$ is computed as the number of events in bin (E_C, θ) divided by the total number of simulated events. This step takes a negligible amount of computation time compared to the MC production. The resulting system matrix (Fig. 3) is stored in a 2D histogram with x-axis corresponding to 50 E_C bins from 0 keV to 400 keV for ^{213}Bi and to 200 keV for ^{221}Fr, and with y-axis corresponding to 180 θ bins from 0° to 180°. We approximate the system matrix to be independent of the gamma ray emission position (i.e. j-bin), so only the elements corresponding to the central bin are calculated. This is demonstrated to be a good approximation by the final performance of our approach. The variations of ε_j within the central 60mm × 30mm × 60mm are below 20% and the maximum drop of 50% occurs at the detector's edge. Since the variations in the main imaging region are considered small, ε_j is assumed constant for simplicity. This is calculated as the total number of detected gamma rays that pass the event selection divided by the total number of produced gamma rays. The precalculated A_j and ε_j are used as look-up tables by the reconstruction algorithm. This process is repeated for the two relevant energies (218 keV and 440 keV).

We further speed up LM-OSEM using GPU acceleration. Each λ_j is computed in a different core of an NVIDIA TITAN RTX graphics card, accelerating the algorithm by more than two orders of magnitude with respect to a single CPU. A_j, ε_j, and the datasets are stored in the GPU memory to reduce memory read and write operations. We further accelerate the algorithm by reducing the voxel space after every iteration, ignoring voxels whose activity drops below 1% of the maximum voxel activity. The demonstration that the impact of this approximation is negligible is given in the Appendix.

B. Proximity imaging

The basic principle of proximity imaging is that the location of a point source can be inferred by the dependence of the gamma ray flux with the inverse of the square root of the distance between the source and the detection point. This technique has demonstrated a spatial resolution of ~2 cm in planar images of 140 keV gamma rays from ^{99m}Tc by using a simple geometric mean reconstruction [35]. Gamma ray direction information is not available for this modality, and the imaging power comes exclusively from the density distribution of the detected gamma rays (Fig. 2).

1) Proximity event selection: The only requirement for proximity imaging is the identification of the location of a gamma interaction in one of the scatterers. Given that proximity imaging requires the detector to be very close to the subject to reach a good spatial resolution, we do not consider PA events in the absorbers. In order to reduce the scattering background, we select PA events by requiring single-pixel events with a deposited energy compatible with the expected gamma ray energy (larger than 430 keV and 200 keV for ^{213}Bi and ^{221}Fr, respectively).

2) OSEM for proximity imaging: A non-list mode OSEM [44] is applied for proximity imaging. Sinograms are defined as the number of gamma rays detected in pixel i for both scatterers. The activity λ_j^{k+1} in voxel j is calculated iteratively by the expression

$$\lambda_j^{k+1} = \frac{\lambda^k}{\chi_j} \sum_{N_i} \frac{M_{ij}}{\sum_l M_{il} \lambda_l^k},$$

(4)

where M_{ij} is the proximity system matrix, defined as the probability of detecting in pixel i a gamma ray produced in voxel j, χ_j is the proximity sensitivity, or probability of detecting a gamma ray from voxel j, and N_i is the total number of bins in the sinogram (which corresponds to the number of total number of pixels in the two scatterers).

In a similar fashion than previously, we calculate M_{ij} and χ_j by MC simulations. We simulate 4×10^9 gamma rays generated along the Y-axis at the center of the detector and the proximity event selection (Sec. III-B1) is applied. We rely on the fact that M_{ij} is symmetric under XZ translations in order to build a look-up table with only events produced along the Y axis. M_{ij} is calculated by translating the XZ coordinate to be at the center of the XZ coordinate of voxel j. Since χ_j varies little within the imaging region, we consider it constant, calculated as the total number of gamma rays passing the proximity event selection divided by the total number of generated gamma rays. M_{ij} and χ_j are computed for the two relevant energies (440 keV and 218 keV). Values of M_{ij} are given by interpolating the look-up table values. The algorithm is accelerated by ignoring voxels whose activity drops below 1% of the maximum voxel activity after every iteration.

IV.   System optimization and characterization

This section is dedicated to optimizing the detector and reconstruction parameters, and evaluating the system's performance. Unless otherwise specified, the parameters used in the figures are fixed to the nominal values shown in Table I.

A.   Detector parameters

In this section we optimize the CZT thickness, the distance between the scatterer and the absorber, and the pixel size in order to maximize the sensitivity for each modality and to enhance the angular resolution of Compton imaging. We also discuss the dependence of imaging performance with DOI and energy resolution and justify our chosen values.

1)   Detector thickness: For a fixed-size detector, the CZT thickness is the dominant component of the sensitivity. We simulate an isotropic point source at the center of the detector and vary the thickness of one of the elements while fixing the other one. The Compton and proximity sensitivities given by the event selection criteria (Secs. III-A1 and III-B1) are shown as a function of CZT thickness for scatterer and absorber in Fig. 4. Since proximity does not use the absorber, only its dependence with the scatterer's thickness is shown. The Compton sensitivity is proportional to the absorber's thickness, due to the increased stopping power. Regarding the scatterer, the sensitivity in Compton coincidence events reaches a maximum for 3 mm thickness for ^{221}Fr and 8 mm for ^{213}Bi. The Compton sensitivity falls off at larger thicknesses because the probability of a gamma ray being absorbed in the scatterer after a Compton interaction increases. The proximity sensitivity monotonically increases with scatterer thickness, as expected given the higher stopping power. We choose 6 mm as the optimal thickness since it provides a Compton sensitivity above 1 % for both energies and isotopes, and since 6 mm-think CZT detectors are readily available from commercial sources.

2)   Distance between scatterer and absorber: The distance between the scatterer and the absorber also affects the Compton sensitivity and it also plays an important role on the angular resolution of Compton imaging. The sensitivity to point sources at the center of the detector as a function of the distance is shown in Fig. 4, where we observe that it decreases with distance. On the other hand, the angular uncertainty improves with distance, as shown in Fig. 5 for point sources at the center. The angular uncertainty is defined as

$$\Delta\theta = \sqrt{(\Delta\theta_c)^2 + (\Delta\theta_d)^2}, \tag{5}$$

where θ_c is the uncertainty on the determination of the Compton angle and θ_d is the uncertainty in the determination of the direction of the scattered gamma ray, $\vec{r}_{PA} - \vec{r}_C$ (Fig. 2). The former is calculated as the FWHM of the distribution of the difference between the Compton angle from Eqn. (2) and the true Compton angle, defined as the scattering angle given by the gamma ray trajectories in the MC simulation. The latter is calculated as the FWHM of the difference in the detected direction of the scattered gamma ray, $\vec{r}_{PA} - \vec{r}_C$, and its true direction. We choose to model a distance of 25 mm, which is the

first point in the plateau region (Fig. 5), with angular uncertainties of $(5.10 \pm 0.10)°$ and $(10.70 \pm 0.45)°$ for ^{213}Bi and ^{221}Fr, respectively.

3) Pixel size: The size of the pixel further determines the angular uncertainty. We compute the angular uncertainty (Eqn. (5)) as a function of the pixel size. As shown in Fig. 5, this is rather constant for pixel sizes between 1 mm and 4 mm. We set 1 mm as the default value of our detector model.

4) Depth of interaction: The dependence of the angular uncertainty with DOI is shown in Fig. 5, where a very mild dependence is observed. We choose to model a DOI of 1 mm FWHM, which improves the angular uncertainty to $(4.20 \pm 0.15)°$ and $(10.10 \pm 0.21)°$ for ^{213}Bi and 221Fr, respectively.

5) Energy resolution: The energy resolution is a critical parameter for Compton imaging that plays a major role in its angular uncertainty, as shown in Fig. 5. CZT has demonstrated excellent energy resolutions of 2.56 % at 276 keV and 1.96 % at 383 keV [45]. We choose 6.5% FWHM at 122 keV, a typical value provided by vendors like Redlen Technologies, to model our detector's energy response.

B. Reconstruction parameters

In this section we compute the spatial resolution of each modality as a function of the reconstruction parameters, namely, the voxel size, the number of subsets and the number of iterations, using a point source at the center of the detector. We define the spatial resolution as the resolution on the XZ plane (landscape). We calculate it by projecting the reconstructed image on the XZ plane, finding the FHWM contour, and taking the average of the distance between the true position of the point source and sample points over the FWHM contour.

1) Voxel size: The spatial resolution depends on the voxel size and the speed of the reconstruction depends on the total number of voxels. Since the voxel size determines the total number of voxels for a fixed imaging volume, this introduces a trade-off between performance and speed. We compute the spatial resolution as a function of the voxel's edge length for cubic voxels in Fig. 6. The spatial resolution for both modalities plateaus at a voxel size of ~2 mm, so choosing voxels this size or smaller would not jeopardize the image reconstruction. Since the voxel size is optimized for Compton and proximity independently, the chosen values are different and correspond to 1.5 mm for Compton imaging and 2.0 mm for proximity (Table I), unless otherwise noted.

2) Number of subsets and iterations: Increasing the number of subsets accelerates convergence of the EM algorithm almost linearly, but it enhances noise since it reduces the number of events in each subset [44]. We compute the spatial resolution as a function of the number of iterations and subsets for each modality (Fig. 7). Overall, the spatial resolution obtained after a single OSEM iteration with *n* subsets, is equivalent to *n* iterations of MLEM. For this case with a point source, the region of constant spatial resolution is reached for Compton or proximity reconstructions with 10 subsets and after 10 iterations.

The optimal number of subsets and iterations is evaluated empirically case by case, since it strongly depends on the size of the subject, the distribution of the activities, and the number of detected counts. A large number of iterations and subsets is not recommended since they can cause noise enhancement, so we generally keep these numbers low in all cases.

C. Reconstruction performance evaluation with a point source

The spatial resolution of the final optimal detector (Table I) is calculated as a function of the distance from the scatterer by varying the Y position of a point source (Fig. 8). The best Compton spatial resolution (FWHM) that we achieve is (1.56 ± 0.05) mm for ^{221}Fr and (1.58 ± 0.03) mm for ^{213}Bi for a point source at 0.5 mm from the scatterer, and the poorest spatial resolution is (3.28 ± 0.41) mm for ^{221}Fr and (1.61 ± 0.02) mm for ^{213}Bi, for a point source at the center of the detector (15.5 mm from the scatterer). For proximity imaging, the best resolutions are (2.88 ± 0.01) mm for ^{221}Fr and (3.22 ± 0.02) mm for ^{213}Bi, and the poorest are (10.90 ± 2.38) mm for ^{221}Fr and (9.17 ± 2.48) mm for ^{213}Bi.

These values do not imply that these modalities can resolve point sources at distances larger than the estimated spatial resolution, since this also depends on the signal-to-noise ratio of the specific images given for each modality, but they serve as figures-of-merit for a first-order evaluation of the image reconstruction. The imaging performance with distributions more complex than a point source is evaluated and discussed in Sec. V.

The speed of the reconstruction algorithms is evaluated and shown in Fig. 9. Our GPU-accelerated LM-OSEM implementation can process an image at about ~3 μs per voxel and per event, when the number of voxels and events are larger than ~ 2000. This is almost three orders of magnitude faster than our implementation of LM-OSEM in a single CPU, which takes ~2 ms per voxel and event. For proximity imaging, OSEM is less compute-intensive than LM-OSEM since it is independent on the number of events, so we did not implement GPU acceleration. The speed performance of OSEM is shown in Fig. 9.

V. Imaging results

The imaging capabilities of our system are tested with the simulation of two hot rod phantoms and a realistic mouse phantom for different activity scenarios.

A. Extremely low activity phantoms

Images of a micro-Derenzo phantom with 4 μCi and 1 μCi of ^{225}Ac are reconstructed using Compton imaging. The phantom consists of a 30 mm diameter acrylic cylinder and 1 mm thickness, with 6 different sets of rods of diameters 3 mm, 2.5 mm, 2 mm, 1.5 mm, 1 mm and 0.5 mm (Fig. 10). We simulate two different locations for the phantom: one at 1.0 mm from the scatterer's front face, and another at 15.5 mm (detector center). We simulate an exposure of 15 minutes as a representative value of preclinical in vivo imaging conditions, which ranges between exposures of a few minutes to ~ 90 minutes. Compton images using 30 subsets and 10 iterations can resolve the 1.5 mm rods in all cases when the phantom is at 1 mm from the detector. The poorest resolution is obtained at the center of the detector, where the reconstructed images can resolve the 2 mm rods for 4 μCi and the 2.5 mm rods for 1 μCi for ^{213}Bi. Overall, the imaging performance for ^{221}Fr and ^{213}Bi gets worse as the

phantom moves away from the detector and as the activity is lowered (Fig. 10). ^{221}Fr images are degraded at the detector center, where none of the rods can be clearly distinguished for such low activities.

The structure of the micro-Derenzo phantom cannot be resolved by our current proximity reconstruction for the explored activities, thus, we evaluate its performance with a different phantom. We defined an acrylic phantom with 3 pairs of rods of 3 mm, 2 mm and 1 mm diameter filled with water and at distances 2 cm, 1.5 cm and 1 cm from each other, respectively (Fig. 11). The thickness of the phantom is 1 mm and it is located at 1 mm from the top scatterer's front face. Proximity imaging identifies and resolves every volume for a total activity of 0.1 μCi (an order of magnitude lower than for Compton imaging of the micro-Derenzo phantom) and an exposure of 15 minutes (Fig. 11) for both ^{221}Fr and ^{213}Bi.

B. Realistic simulation of mouse in vivo

A mouse phantom (MOBY 2.0 [37]) is simulated with 0.5 μCi of ^{225}Ac equally distributed in the brain, spleen and muscle (0.167 μCi each). This provides a realistic scenario with a high activity and localized region (spleen), a medium activity and more extensive region (brain), and a low activity region that plays the role of a warm background (muscle) (Fig. 12). After a 15-minute exposure, the Compton reconstruction provides 3D images with a single bed position, with projections shown in Fig. 12 compared to the ground truth distributions. The ZX plane shows the spleen and brain regions clearly resolved for both ^{221}Fr and ^{213}Bi, with some reconstruction artifacts at negative Z values. The organs can also be resolved in the Y coordinate even without a lateral view. Resolution on the Y coordinate could be improved by a second detector view with the detector rotated 90° along the Z axis, although we do not explore that option on this paper.

The proximity imaging reconstruction is applied to the same mouse phantom simulation but with a shorter exposure of 5 minutes. Proximity images show the ability to resolve both organs, obtaining a better quality image for ^{221}Fr than for ^{213}Bi, given the much higher sensitivity of the latter. Due to this reason, noise is enhanced in the ^{213}Bi case with respect to the ^{221}Fr case, which justifies the lower number of OSEM iterations.

VI.   Discussion

We predict that our CZT detector can deliver 3D images of the ^{225}Ac daughters (^{221}Fr and ^{213}Bi) for very low doses of 0.5 μCi with 15 minutes exposures and a single bed position using Compton imaging. Additionally, proximity imaging, enabled by a high-Z CZT scatterer, can provide planar images of the same isotopes and dose in 5 minutes. Below, we discuss the relevance and limitations of these results and put them into context.

A.   Relevance of our results

Preclinical in vivo imaging is extremely important for drug development (Sec. I) since they provide quantitative PK distributions of radiopharmaceuticals during treatment. Since quantitative preclinical in vivo imaging of TAT is not available, PK studies are currently done ex vivo by dissecting tumors and organs and measuring their dose independently in a gamma ray counter with no spatial sensitivity [22]. This provides organ-level distributions of

the location of the TAT radiopharmaceuticals. For TAT imaging to outperform and substitute this current methodology, it requires to deliver 3D information with a spatial resolution better than the typical size of the organs, i.e., a few millimeters. Another important requirement is that imaging should be performed well under an hour, in order to prevent from morbidity, and also to enable scanning of large mice cohort for statistically significant studies. In this manuscript, we predict that our system meets those requirements for ^{225}Ac (Sec. V).

Our approach has been tested with a realistic mouse phantom for a specific dose distribution. In real scenarios, the radiopharmaceutical distribution would greatly vary case by case and it is impossible to cover all the cases in this paper. The problem can be reduced by arguing that the relevant parameters are the size and shape of the organ, the activity density, and the distance with respect to the detector. We chose to image brain and spleen over a muscle (warm) background as a representative case that covers different sizes, shapes, activity densities and locations. Additionally, the phantom studies at two different depths provides a detector characterization that attempts to cover most of that parameter space.

The MOBY phantom [37] represents a very precise mouse anatomy, used in a number of simulation studies. Discrepancies with real mice anatomy come from small variations in organ composition, mass, volume, mouse size, and mouse position at the time of imaging. Organ motion is also an important source of variations, which can be simulated using the dynamic feature of the MOBY phantom, although the present study only consider a static model. Our study should be considered a demonstration of the concept with a representative case.

This paper presents the first study and comparison of Compton and proximity imaging in the same digital phantoms. We show that proximity imaging achieves much higher sensitivities than Compton imaging and can acquire images of low activity phantoms with doses as low as 0.1 µCi (Sec. V). Sensitivity and performance decreases with energy for proximity imaging while it increases with energy for Compton imaging (Sec. V). Thus, proximity presents a complementary technique to Compton imaging and it is very effective in scenarios where imaging needs to be performed extremely fast (e.g., dynamic SPECT [46]) and a good spatial resolution is not essential. In addition, this complementary response suggests that the combination of both methods could improve the sensitivity and spatial resolution given by each modality separately. The major limitation of Compton imaging is its poorer performance under 300 keV [32, 33]. Since we predict that proximity behaves better at lower energies, the combination of Compton and proximity could provide a better performance. However, we consider that possibility out of the scope of the current study and we leave it for future papers.

A major limitation of proximity imaging is the poor resolution in depth perception [34, 47]. We achieve a depth resolution of 15 mm, which corresponds to the size of the voxel dimension Y (2 voxels in a 30 mm-width image space). Alternatives to the standard OSEM algorithm that improve the spatial resolution and the ability to resolve complex distributions have been explored [47, 48] and could be a promising future addition to this analysis.

Additionally, algorithms based on likelihood priors (e.g., maximum a posteriori algorithms [49]) could provide a better depth perception for proximity imaging and enable tomography.

The application of our apparatus could also be extended to imaging of other TAT radionuclides like ^{227}Th, ^{211}At or ^{213}Bi, given their similar gamma-ray emission energies and injected doses [14], although in this paper we only explore ^{225}Ac since it is the most promising one [2].

B. Comparison with other studies

The only in vivo preclinical TAT imaging modality that has been demonstrated is CLI [13]. Our approach presents several advantages over that technique. First, separation of the ^{221}Fr and ^{213}Bi signals is possible, as opposed to CLI, that is not sensitive to the type of radionuclide. This enables PK study of each ^{225}Ac daughter by separate, which is crucial to infer if radionuclide detachment occurs and at what point in the decay chain [8–10]. Second, we provide 3D images instead of 2D images. And third, the sensitivity and spatial resolution of CLI degrades with source depth much more rapidly than for gamma-ray imaging. This is due to the Cherenkov attenuation in tissue being much higher than that of gamma rays.

Other promising work is been developed regarding gamma ray imaging of ^{225}Ac. A new concept of high-sensitivity multi-pinhole collimator dedicated to TAT imaging [23] could meet the requirements, although in vivo imaging with submicrocurie doses is still to be demonstrated. In [36], the authors propose a Compton camera using GAGG to image ^{221}Fr and ^{213}Bi from ^{225}Ac. Their tested activities (~MBq/ml) are three orders of magnitude higher than our targeted activities (~kBq/ml). Their detection efficiency (~10^{-5}) is three orders of magnitude lower than ours, partially due to the thicker GAGG scatterer, which lowers the number of photons that escape the scatterer. For similar exposure times, we achieve a spatial resolution of about 2 mm, as opposed to their spatial resolution of the order of centimeters.

Other Compton camera systems have been proposed in [24–30, 50]. The particular difference of our approach is that we focus on maximizing the sensitivity, which is predicted to be one or two orders of magnitude larger than those. We achieve this by using CZT, that has a balanced Compton and PA cross-sections, by optimizing the thickness of the detector to minimize scatterer absorption (Fig. 4), and by using a larger detector design and locating it very close to the subject.

C. Detector modeling considerations

In this section we highlight and justify the main assumptions and approximations made to model the detector's response.

We assumed the CZT detection efficiency to be 100%. This is based on the fact that, for relatively thin detectors, the small-pixel effect [51] makes the efficiency very close to maximal, except for interactions very close to the anode. In [52], the inefficiency for 1 mm-pixel detectors were modeled and estimated to be over 90% for more than 80% of the crystal interaction depths. Furthermore, correction methods based on the depth of interaction can be introduced to increase detection efficiency [53]. In the least favorable case of an

absolute CZT efficiency of 80%, our results would still hold if the exposure times are increased by 25% for proximity imaging and 44% for Compton imaging, bringing the final exposure time to 6 minutes for proximity and 22 minutes for Compton imaging. This is still well within the in vivo preclinical TAT imaging requirements.

The modeled energy resolution (6.5% at 122 keV) is considered a conservative value since it is guaranteed by commercial CZT manufacturers (e.g., Redlen Technologies) and it has been largely improved in recent CZT systems [45, 54].

The simulated DOI resolution (1 mm FWHM) is conservative since ~0.05 mm FWHM has been demonstrated for 1-cm thick CZT detectors [55] and 5-mm detectors [56] at 662 keV. DOI resolution requires dual readout, which increases the amount of dead material in between detectors and could decrease sensitivity. We show that DOI resolution is desirable but not critical (Sec. IV-A4), so it can be optional if its adoption is technically challenging.

We only considered the dominant gamma-ray emissions since their branching ratio are two orders of magnitude larger than the secondary gamma-ray emissions. X rays are not simulated since they lay well below the considered energy windows.

Alternatives to CZT as a scatterer material are scintillator detectors (e.g., NaI, CsI, BGO or GAGG) and other solid-state detectors (e.g. high-purity Ge). Since solid-state detectors do not require an intermediary (photosensor) to extract the signal, it minimizes the amount of dead material with respect to scintillator detectors. This is especially important for Compton cameras to minimize the photon interaction in inactive detector parts between the scatterer and the absorber. Ge detectors typically require cooling and a cryostat [57], which does not allow to easily place the scatterer very close to the subject as required by proximity imaging. The role of CZT as a high-Z scatterer is also critical, since it provides a relatively large Compton interaction rate and, at the same time, allowing for those photons to escape and to reach the absorber. Compared to GAGG [36], CZT outperforms its sensitivity, partially due to this reason. The superb energy resolution of CZT (better than most traditional scintillators [58]) is also required to obtain a high spatial resolution for Compton imaging. Regarding CZT as a absorber material, its sensitivity could be improved by a higher stopping power detector like GAGG or BGO, given that excellent energy resolution is not a requirement for the absorber. This could lead to even higher sensitivities and lower exposure times. Since our CZT-CZT design already meets the TAT imaging requirements, we have not explored alternative absorber materials.

D. Potential for human translation

Clinical imaging of TAT would represent a window to more personalize treatments and alpha theranostics. Yet, they face similar challenges than preclinical imaging, namely, extremely low doses and relatively high gamma-ray energies. These are problems that our proposed apparatus is predicted to overcome in preclinical settings. Nevertheless, the main limitation of our apparatus is related to the size of the subject. Compton imaging quickly degrades with distance, and proximity imaging is only efficient when the subject is very close to the detector. For these reasons, whole-body clinical imaging does not seem practical as presented here. However, there could be promise for organ-dedicated purposes, where the

field of view is smaller (e.g., brain), or when the tumors are localized (e.g., sentinel lymph nodes for melanoma or breast cancer [59]).

VII. Conclusion

We have presented the design of a CZT gamma camera that enables both Compton and proximity imaging of extremely low ^{225}Ac activities in order to obtain the biodistributions of ^{221}Fr and ^{213}Bi in vivo, a current unmet need in preclinical imaging of developmental TAT radiopharmaceuticals. The camera's performance predicted by our dedicated GEANT4 simulations shows that Compton imaging can resolve features of up to 1.5 mm for 221Fr and 213Bi for activities as low as 1 μCi. Proximity reconstruction can resolve two 1 mm point sources at 1 cm distance for extremely low activities (below 0.1 μCi) and a 15-minutes exposure. A realistic mouse phantom simulation reveals that the brain and the spleen can be clearly differentiated in the presence of a warm background (muscle) for a 0.5 μCi intake of ^{225}Ac, for both ^{221}Fr and ^{213}Bi, and for Compton and proximity imaging, with exposures of 15 and 5 minutes, respectively. This paper provides a theoretical proof, based on MC simulation, that our Compton-camera could fulfill the demanding requirements for in vivo preclinical TAT imaging.

Acknowledgments

Appendix

To accelerate our reconstruction algorithm, voxels whose activity fall below 1% the maximum voxel activity are ignored after every iteration. We show the impact of this approach by comparing images obtained with and without this method. In Fig. 14, a Derenzo phantom with 1 μCi located at the center of the detector is reconstructed with and without using this technique. Both images are virtually the same.

References

[1]. Parker Chris C. et al. "Targeted Alpha Therapy, an Emerging Class of Cancer Agents: A Review". In: JAMA Oncology 4 (2018), pp. 1765–1772. [PubMed: 30326033]

[2]. Tafreshi Narges K. et al. "Development of Targeted Alpha Particle Therapy for Solid Tumors". In: Molecules 24.23 (2019). ISSN: 1420–3049.

[3]. Pouget Jean-Pierre et al. "Clinical radioimmunotherapy—the role of radiobiology". In: Nature reviews Clinical oncology 8.12 (2011), pp. 720–734.

[4]. Scheinberg David A and McDevitt Michael R. "Actinium-225 in targeted alpha-particle therapeutic applications". In: Current radiopharmaceuticals 4.4 (2011), pp. 306–320. [PubMed: 22202153]

[5]. Kratochwil Clemens et al. "225Ac-PSMA-617 for PSMA-targeted a-radiation therapy of metastatic castration-resistant prostate cancer". In: Journal of Nuclear Medicine 57.12 (2016), pp. 1941–1944. [PubMed: 27390158]

[6]. Kratochwil Clemens et al. "Targeted α-therapy of metastatic castration-resistant prostate cancer with 225Ac-PSMA-617: dosimetry estimate and empiric dose finding". In: Journal of Nuclear Medicine 58.10 (2017), pp. 1624–1631. [PubMed: 28408529]

[7]. Janoki GA and Kerekes A. "Pharmacokinetics of radiopharmaceuticals." In: Acta Physiologica Hungarica 79.2 (1992), pp. 183–196. [PubMed: 1304681]

[8]. Roscher Mareike, Bakos Gábor, and Benešová Martina. "Atomic Nanogenerators in Targeted Alpha Therapies: Curie's Legacy in Modern Cancer Management". In: Pharmaceuticals 13.4 (2020). ISSN: 1424–8247.

[9]. De Kruijff Robin M, Wolterbeek Hubert T, and Denkova Antonia G. "A critical review of alpha radionuclide therapy—how to deal with recoiling daughters?" In: Pharmaceuticals 8.2 (2015), pp. 321–336. [PubMed: 26066613]

[10]. Kozempel Ján, Mokhodoeva Olga, and Vlk Martin. "Progress in targeted alpha-particle therapy. What we learned about recoils release from in vivo generators". In: Molecules 23.3 (2018), p. 581.

[11]. Borchardt Paul E. et al. "Targeted Actinium-225 in Vivo Generators for Therapy of Ovarian Cancer". In: Cancer Research 63.16 (2003), pp. 5084–5090. ISSN: 0008–5472. eprint: https://cancerres.aacrjournals.org/content/63/16/5084.full.pdf. [PubMed: 12941838]

[12]. Salvanou Evangelia-Alexandra et al. "A Proof-of-Concept Study on the Therapeutic Potential of Au Nanoparticles Radiolabeled with the Alpha-Emitter Actinium-225". In: Pharmaceutics 12.2 (2020). ISSN: 1999–4923.

[13]. Pandya Darpan N. et al. "Preliminary Therapy Evaluation of ¡sup¿225¡/sup¿Ac-DOTA-c(RGDyK) Demonstrates that Cerenkov Radiation Derived from ¡sup¿225¡/sup¿Ac Daughter Decay Can Be Detected by Optical Imaging for ¡i¿In Vivo¡/i¿ Tumor Visualization". In: Theranostics 6 (2016), pp. 698–709. [PubMed: 27022417]

[14]. Seo Youngho. "Quantitative Imaging of Alpha-Emitting Therapeutic Radiopharmaceuticals". In: Nuclear medicine and molecular imaging 53.3 (June 2019), pp. 182–188. ISSN: 1869–3474. [PubMed: 31231438]

[15]. Goorden Marlies C et al. "VECTor: a preclinical imaging system for simultaneous submillimeter SPECT and PET". In: Journal of Nuclear Medicine 54.2 (2013), pp. 306–312. [PubMed: 23077113]

[16]. Robertson Andrew KH et al. "Multi-isotope SPECT imaging of the 225Ac decay chain: feasibility studies". In: Physics in Medicine & Biology 62.11 (2017), p. 4406. [PubMed: 28362640]

[17]. Usmani Sharjeel et al. "225Ac Prostate-Specific Membrane Antigen Posttherapy alpha Imaging". In: Clinical Nuclear Medicine 44.Issue 5 (2019), pp. 401–403. [PubMed: 30932973]

[18]. Meltem Ocak et al. "Post-therapy imaging of 225Ac-DOTATATE treatment in a patient with recurrent neuroendocrine tumor". In: European Journal of Nuclear Medicine and Molecular Imaging 47 (2020), pp. 2711–2712. [PubMed: 32123970]

[19]. Vatsa Rakhee et al. "225Ac-PSMA-617 Radioligand Posttherapy Imaging in Metastatic Castrate-Resistant Prostate Cancer Patient Using 3 Photopeaks". In: Clinical Nuclear Medicine 45.Issue 6 (2020), pp. 437–438. [PubMed: 32366786]

[20]. Kamaleshwaran Koramadai Karuppusamy et al. "Whole-body and Single-Photon Emission Computed Tomography/Computed Tomography Postpeptide Receptor Alpha Radionuclide Therapy Images of Actinium 225-Tetraazacyclododecanetetraacetic Acid–Octreotide as a Primary Modality of Treatment in a Patient with Advanced Rectal Neuroendocrine Tumor with Metastases". In: Indian J Nucl Med. 35.Issue 3 (2020), pp. 226–228. [PubMed: 33082679]

[21]. Gosewisch A et al. "Image-based dosimetry for 225Ac-PSMA-I&T therapy using quantitative SPECT". In: European Journal of Nuclear Medicine and Molecular Imaging 48 (2021), pp. 1260–1261. [PubMed: 32959113]

[22]. Moroz Anna et al. "Theranostic targeting of CUB domain containing protein 1 (CDCP1) in pancreatic cancer". In: Clinical Cancer Research 26.14 (2020), pp. 3608–3615. [PubMed: 32341034]

[23]. Zhang Jiajin et al. "Alpha-SPECT: Hyperspectral single photon imaging of targeted alpha-emission therapy". In: Journal of Nuclear Medicine 60.supplement 1 (2019), pp. 311–311. ISSN: 0161–5505. eprint: https://jnm.snmjournals.org/content.

[24]. LeBlanc JW et al. "Experimental results from the C-SPRINT prototype Compton camera". In: 1998 IEEE Nuclear Science Symposium Conference Record. 1998 IEEE Nuclear Science Symposium and Medical Imaging Conference (Cat. No. 98CH36255). Vol. 2. IEEE. 1998, pp. 743–746.

[25]. Sakai Makoto et al. "Compton imaging with 99m Tc for human imaging". In: Scientific reports 9.1 (2019), pp. 1–8. [PubMed: 30626917]

[26]. Tashima Hideaki et al. "3D Compton image reconstruction method for whole gamma imaging". In: Physics in Medicine & Biology 65.22 (2020), p. 225038. [PubMed: 32937613]

[27]. Kabuki Shigeto et al. "Electron-tracking Compton gamma-ray camera for small animal and phantom imaging". In: Nuclear Instruments and Methods in Physics Research Section A: Accelerators, Spectrometers, Detectors and Associated Equipment 623.1 (2010), pp. 606–607.

[28]. Munekane Masayuki et al. "Visualization of biodistribution of Zn complex with antidiabetic activity using semiconductor Compton camera GREI". In: Biochemistry and biophysics reports 5 (2016), pp. 211–215. [PubMed: 28955826]

[29]. Kishimoto Aya et al. "First demonstration of multi-color 3-D in vivo imaging using ultra-compact Compton camera". In: Scientific reports 7.1 (2017), pp. 1–7. [PubMed: 28127051]

[30]. Sakai Makoto et al. "In vivo simultaneous imaging with 99mTc and 18F using a Compton camera". In: Physics in Medicine & Biology 63.20 (2018), p. 205006. [PubMed: 30222127]

[31]. Nakano Takashi et al. "Imaging of 99mTc-DMSA and 18F-FDG in humans using a Si/CdTe Compton camera". In: Physics in Medicine & Biology 65.5 (2020), 05LT01.

[32]. Han Li et al. "Statistical performance evaluation and comparison of a Compton medical imaging system and a collimated Anger camera for higher energy photon imaging". In: Physics in Medicine & Biology 53.24 (2008), p. 7029. [PubMed: 19015578]

[33]. Fontana Mattia et al. "Compton camera study for high efficiency SPECT and benchmark with Anger system". In: Physics in Medicine & Biology 62.23 (2017), p. 8794. [PubMed: 28994664]

[34]. Mitchell Gregory S and Cherry Simon R. "A high-sensitivity small animal SPECT system". In: Physics in Medicine & Biology 54.5 (2009), p. 1291. [PubMed: 19190360]

[35]. Walker Katherine L et al. "Un-collimated single-photon imaging system for high-sensitivity small animal and plant imaging". In: Physics in Medicine & Biology 60.1 (2014), p. 403. [PubMed: 25504038]

[36]. Yoon C et al. "Estimate of the 225Ac Radioactive Isotope Distribution by Means of DOI Compton Imaging in Targeted Alpha Radiotherapy: A Monte Carlo Simulation". In: Journal of the Korean Physical Society 76 (2020), pp. 954–960.

[37]. Segars W Paul and Tsui Benjamin MW. "MCAT to XCAT: The evolution of 4-D computerized phantoms for imaging research". In: Proceedings of the IEEE 97.12 (2009), pp. 1954–1968. [PubMed: 26472880]

[38]. Allison J et al. Recent developments in Geant4 Nuclear Instruments and Methods in Physics Research Section A: Accelerators, Spectrometers, Detectors and Associated Equipment 835, 186–225. 2016.

[39]. Seibert S et al. RAT-PAC is an Analysis Tool. https://rat.readthedocs.io/en/latest/.

[40]. Du Mond Jesse WM. "Compton modified line structure and its relation to the electron theory of solid bodies". In: Physical Review 33.5 (1929), p. 643.

[41]. Caesar E Ordonez Alexander Bolozdynya, and Chang Wei. "Doppler broadening of energy spectra in Compton cameras". In: 1997 IEEE Nuclear Science Symposium Conference Record. Vol. 2. IEEE. 1997, pp. 1361–1365.

[42]. Mackin Dennis et al. "The effects of Doppler broadening and detector resolution on the performance of three-stage Compton cameras". In: Medical physics 40.1 (2013), p. 012402. [PubMed: 23298111]

[43]. Parra Lucas and Barrett Harrison H. "List-mode likelihood: EM algorithm and image quality estimation demonstrated on 2-D PET". In: IEEE transactions on medical imaging 17.2 (1998), pp. 228–235. [PubMed: 9688154]

[44]. Hudson H Malcolm and Larkin Richard S. "Accelerated image reconstruction using ordered subsets of projection data". In: IEEE transactions on medical imaging 13.4 (1994), pp. 601–609. [PubMed: 18218538]

[45]. Chun Sung-Dae et al. "Property of a CZT semiconductor detector for radionuclide identification". In: Journal of Nuclear Science and Technology 45.sup5 (2008), pp. 421–424.

[46]. Ben-Haim Simona and Agostini Denis. Dynamic SPECT: evolution of a widely available tool for the assessment of coronary flow reserve. 2015.

[47]. Zhou J et al. "Maximum a posteriori image reconstruction for a high sensitivity uncollimated small-animal SPECT system". In: Fully 3D Image Reconstruction in Radiology and Nuclear Medicine. 2013, pp. 90–93.

[48]. Zheng Yifan et al. "Collimatorless Scintigraphy for Imaging Extremely Low Activity Targeted Alpha Therapy (TAT) with Weighted Robust Least Squares (WRLS)". In: International Conference on Medical Image Computing and Computer-Assisted Intervention. Springer. 2020, pp. 803–811.

[49]. Qi Jinyi and Leahy Richard M. "Iterative reconstruction techniques in emission computed tomography". In: Physics in Medicine & Biology 51.15 (2006), R541. [PubMed: 16861768]

[50]. Nurdan T Conka et al. "Design criteria for a high energy Compton camera and possible application to targeted cancer therapy". In: Journal of Instrumentation 10.07 (2015), p. C07018.

[51]. Barrett HH, Eskin JD, and Barber HB. "Charge transport in arrays of semiconductor gamma-ray detectors". In: Physical review letters 75.1 (1995), p. 156. [PubMed: 10059139]

[52]. Myronakis Marios E and Darambara Dimitra G. "Monte Carlo investigation of charge-transport effects on energy resolution and detection efficiency of pixelated CZT detectors for SPECT/PET applications". In: Medical physics 38.1 (2011), pp. 455–467. [PubMed: 21361214]

[53]. Bolotnikov Aleksey E et al. "Te inclusions in CZT detectors: New method for correcting their adverse effects". In: IEEE transactions on nuclear science 57.2 (2010), pp. 910–919.

[54]. Abuelhia E, Kacperski K, and Spyrou NM. "Evaluation of scintillators and semiconductor detectors to image three-photon positron annihilation for positron emission tomography". In: Journal of Radioanalytical and Nuclear Chemistry 276.3 (2008), pp. 685–692.

[55]. He Z et al. "3-D position sensitive CdZnTe gamma-ray spectrometers". In: Nuclear Instruments and Methods in Physics Research Section A: Accelerators, Spectrometers, Detectors and Associated Equipment 422.1–3 (1999), pp. 173–178.

[56]. Kim Younghak, Lee Taewoong, and Lee Wonho. "Radiation measurement and imaging using 3D position sensitive pixelated CZT detector". In: Nuclear Engineering and Technology 51.5 (2019), pp. 1417–1427.

[57]. Vetter Kai. "Recent developments in the fabrication and operation of germanium detectors". In: Annu. Rev. Nucl. Part. Sci 57 (2007), pp. 363–404.

[58]. Hutton Brian F, Erlandsson Kjell, and Thielemans Kris. "Advances in clinical molecular imaging instrumentation". In: Clinical and Translational Imaging 6.1 (2018), pp. 31–45.

[59]. Uren Roger F et al. "Imaging sentinel lymph nodes". In: The Cancer Journal 21.1 (2015), pp. 25–32. [PubMed: 25611777]
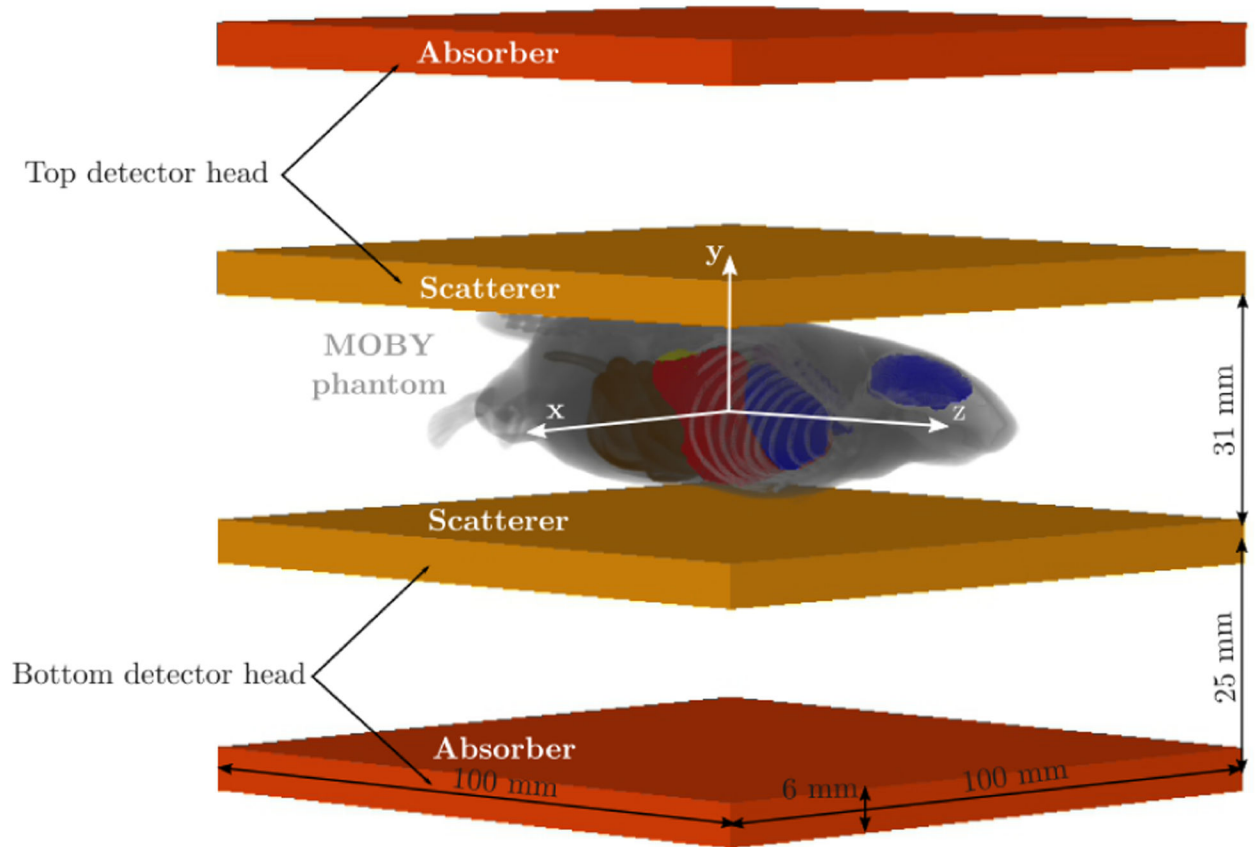
Fig. 1.
Schematic of our CZT detector design with a voxelized model of the MOBY phantom[37], highlighting organs in different colors.
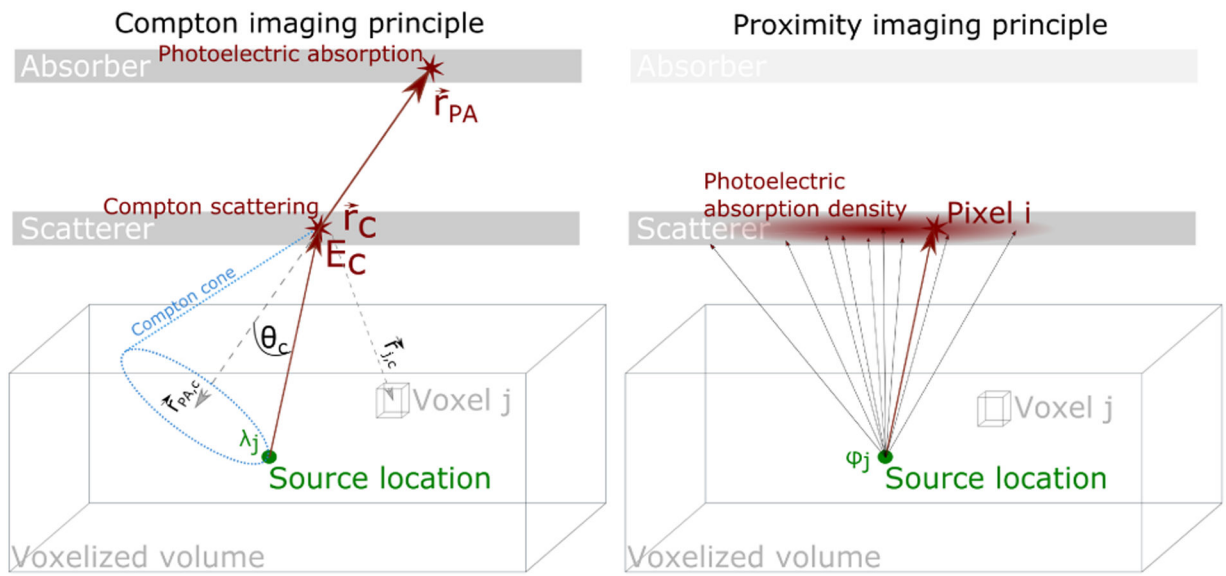
Fig. 2.

Compton (left) and proximity (right) imaging principles. For the latter, the absorber is not used.
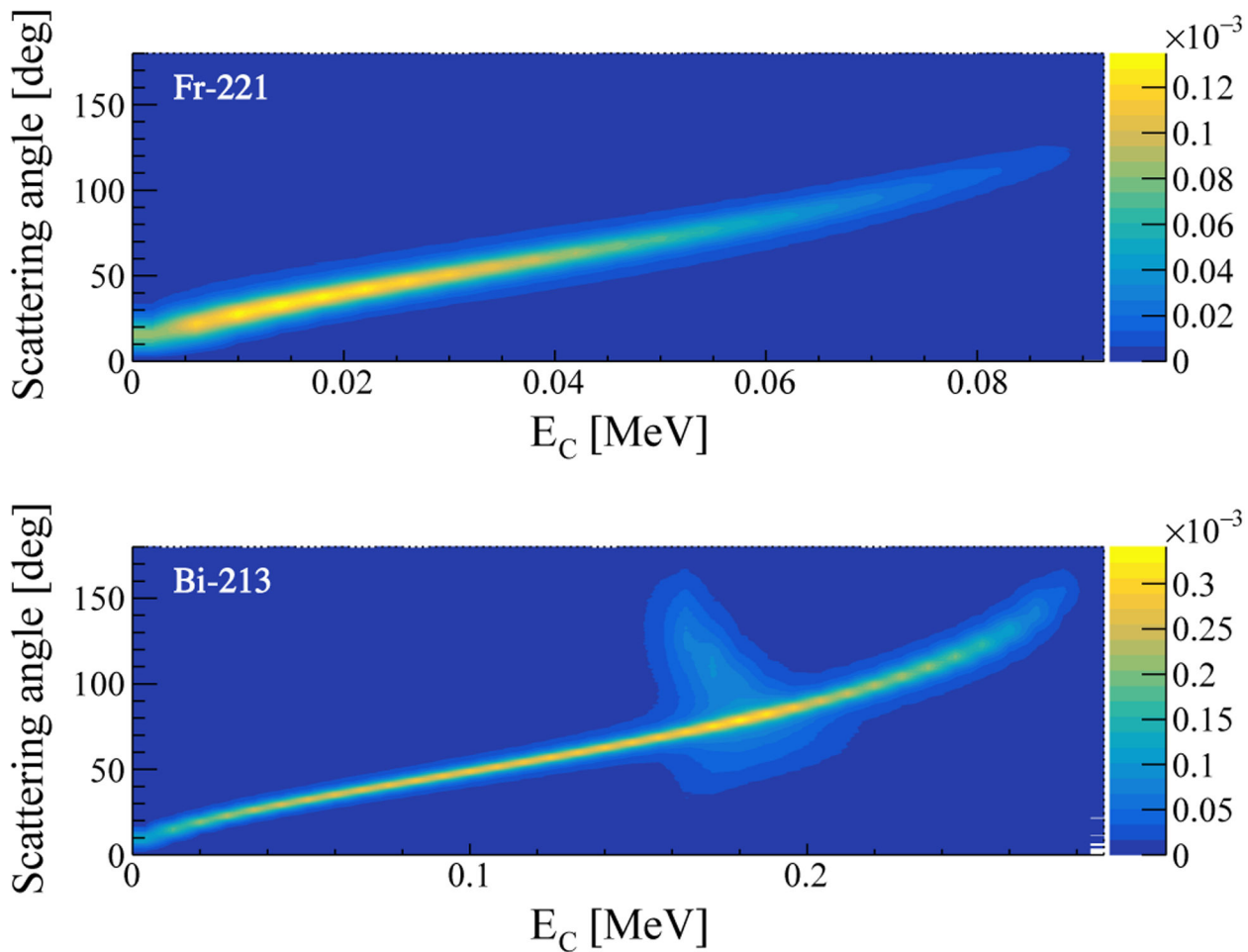
Fig. 3.
Compton scattering probability as a function of the scattering angle (θ) and the energy deposited in the scatterer (E_C) for ^{221}Fr and ^{213}Bi. The feature at 180 keV in the ^{213}Bi figure is due to the back-scattering events, which for ^{221}Fr is beyond the high-energy cut-off.
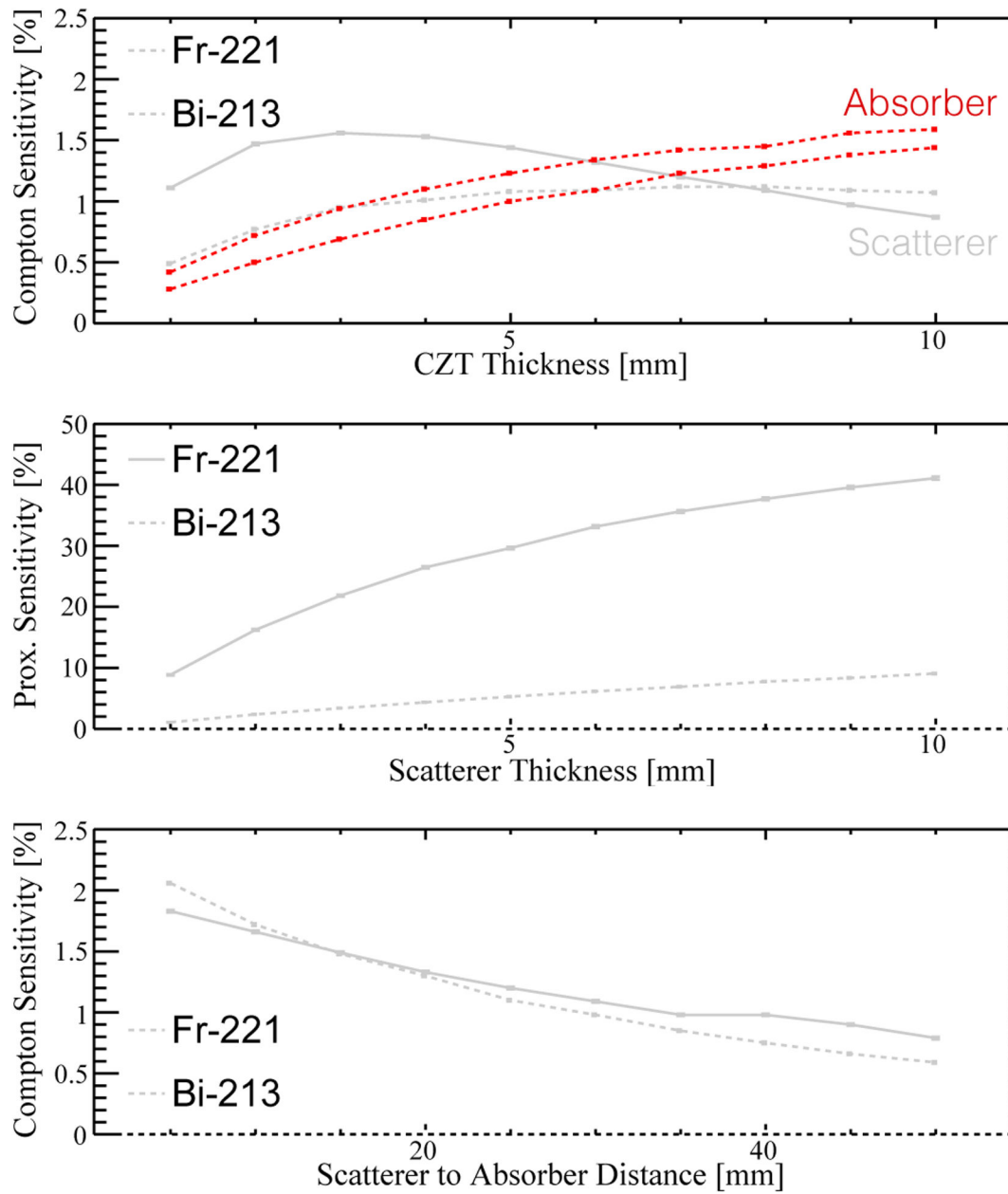
Fig. 4.
Sensitivity to Compton coincidence and proximity events versus CZT detector thickness (top and center) and absorber-scatterer distance (bottom).
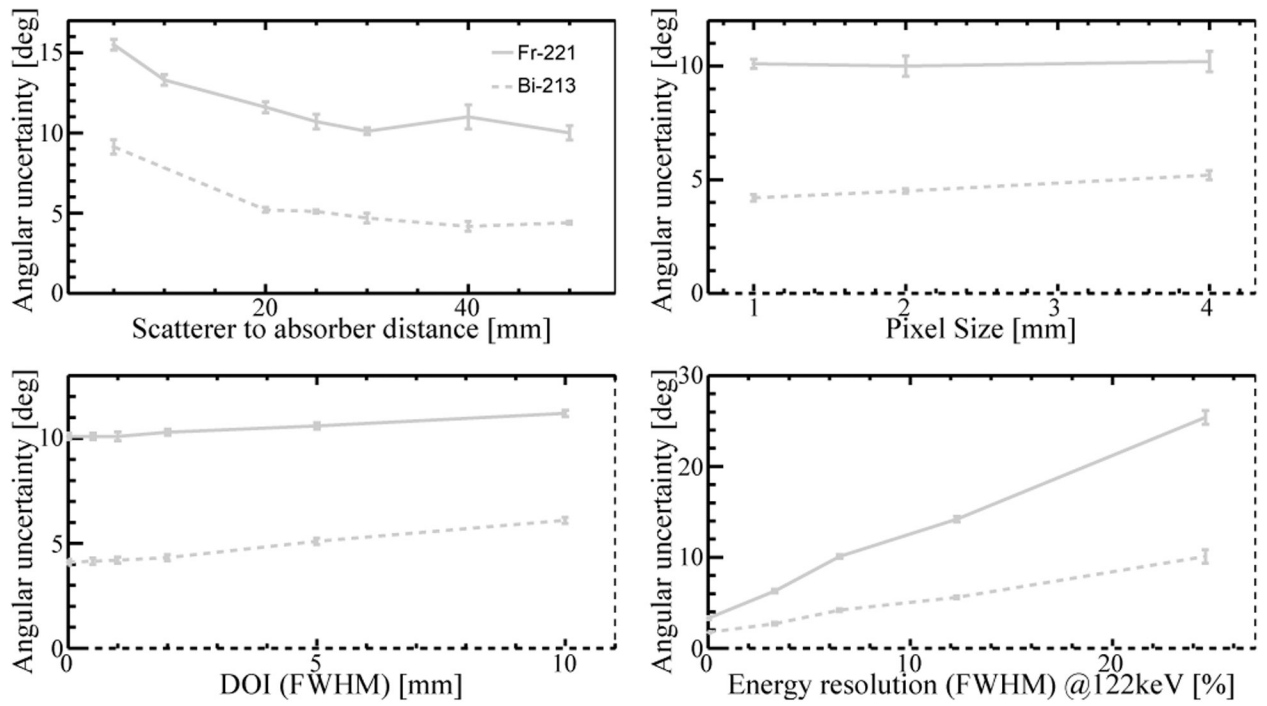
Fig. 5.
Angular uncertainty of Compton imaging versus absorber-scatterer distance (top left), pixel pitch (top right), DOI (bottom left) and energy resolution (bottom right).
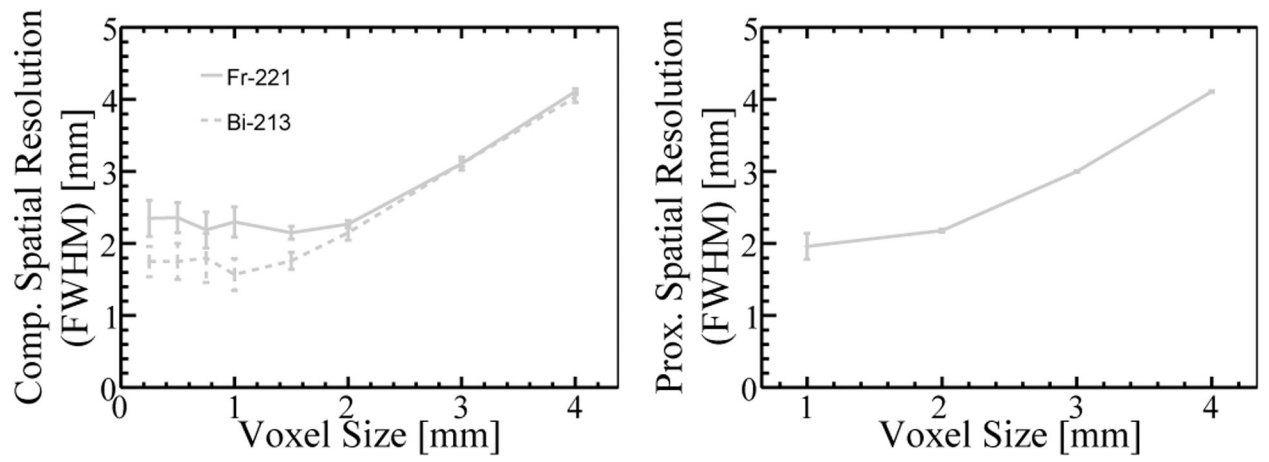
Fig. 6.
Spatial resolution of Compton (left) and proximity (right) imaging versus voxel's size. The curves for ^{221}Fr and ^{213}Bi are overlapping in the proximity spatial resolution plot.
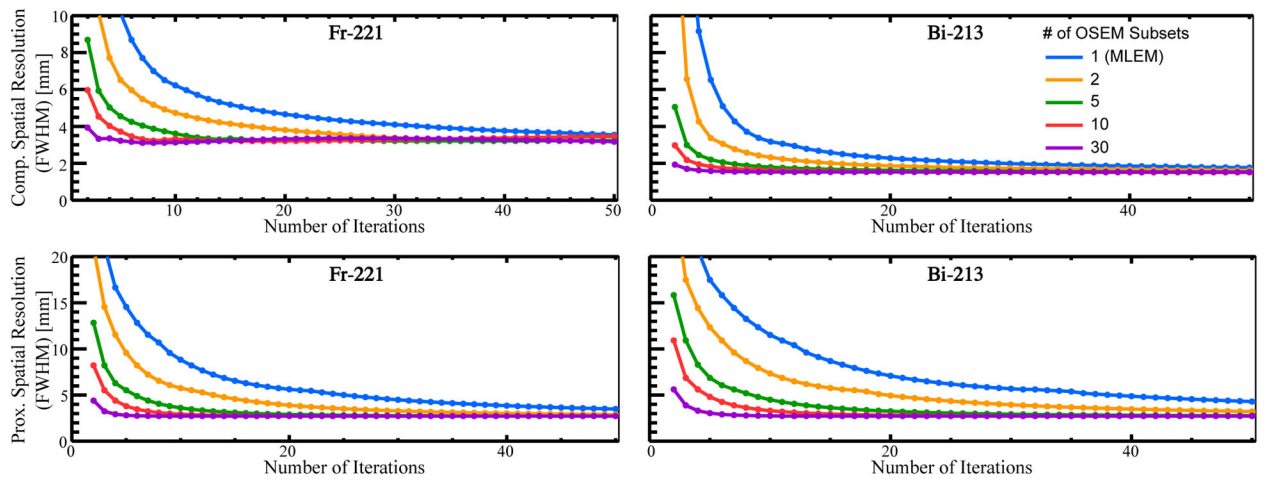
Fig. 7.
Spatial resolution of Compton (top) and proximity (bottom) imaging versus number of iterations and number of OSEM subsets.
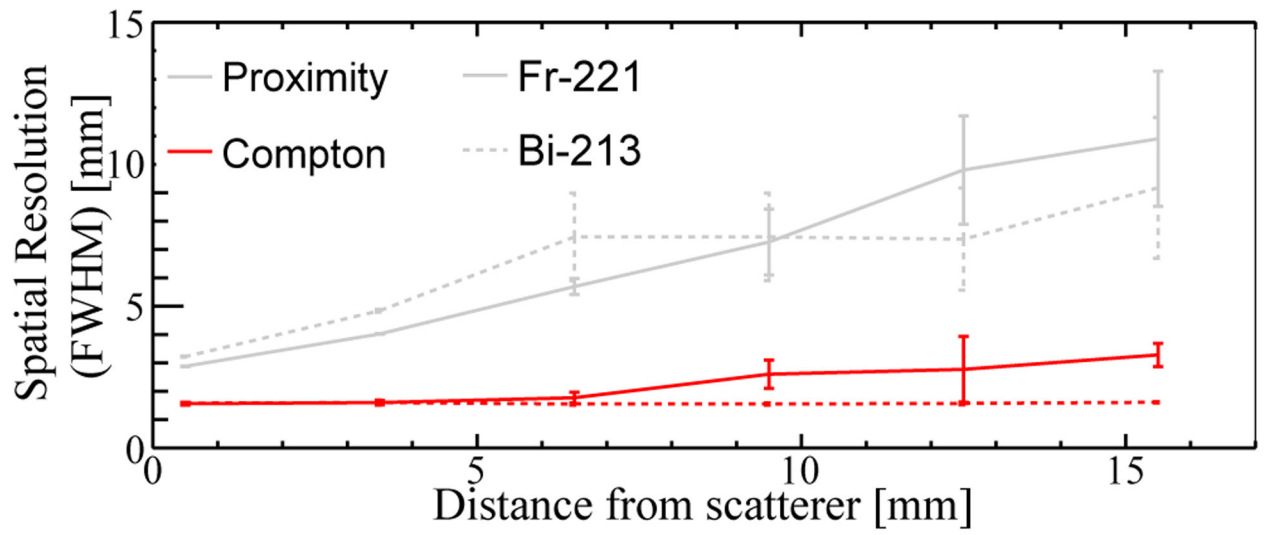
Fig. 8.

Spatial resolution of Compton and proximity imaging as a function of the distance from the scatterer for the optimized detector design (Table I).
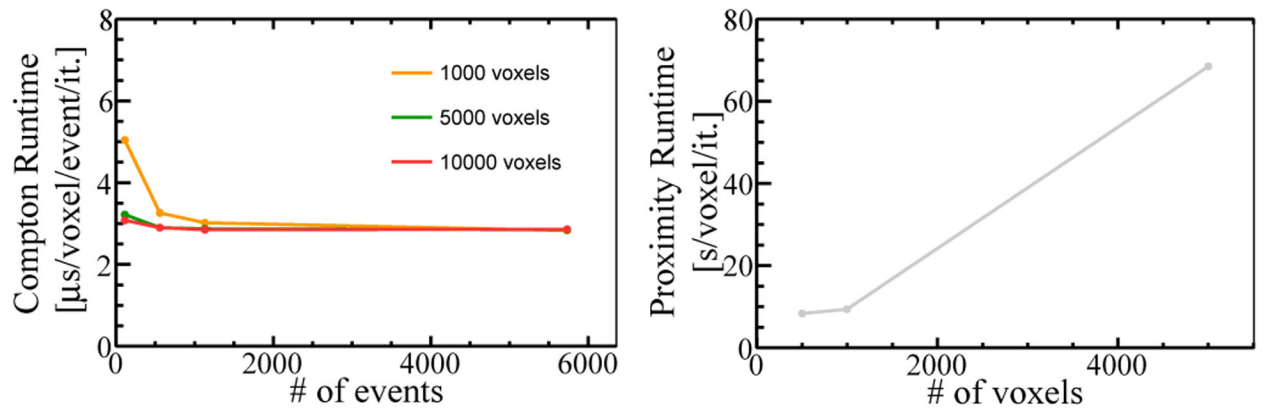
Fig. 9.

Speed of the first iteration of the GPU-accelerated LM-OSEM (left) and OSEM (right) reconstruction algorithms.
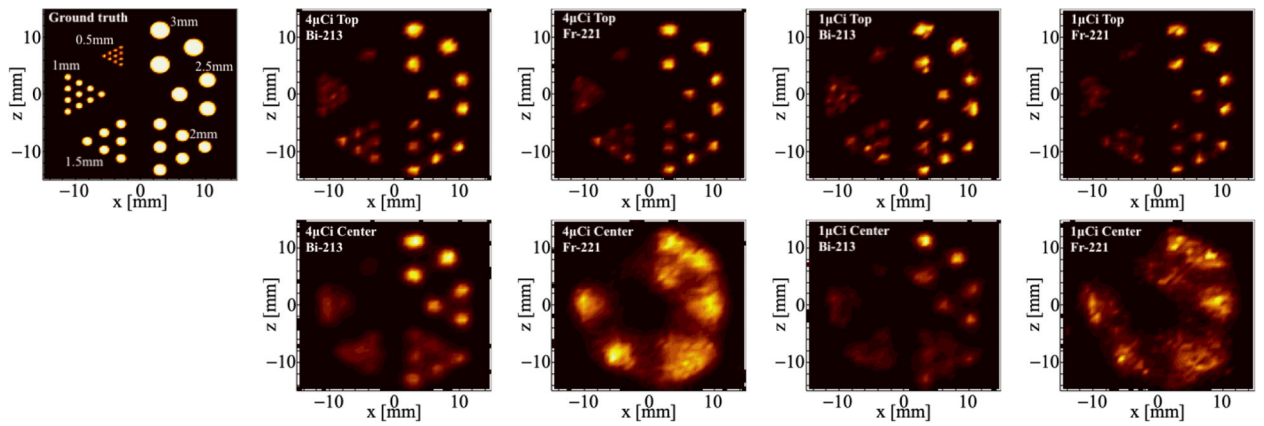
Fig. 10.
Ground truth and Compton-reconstructed images of two micro-Derenzo phantoms with 4 μCi and 1 μCi of ^{225}Ac at two different positions (labeled 'top': 1 mm from top scatterer, and labeled 'center': 15.5 mm from scatterer), for ^{221}Fr and ^{213}Bi. The simulated exposure is 15 minutes. For these images we use 0.75 mm voxels, 30 subsets and 10 iterations.
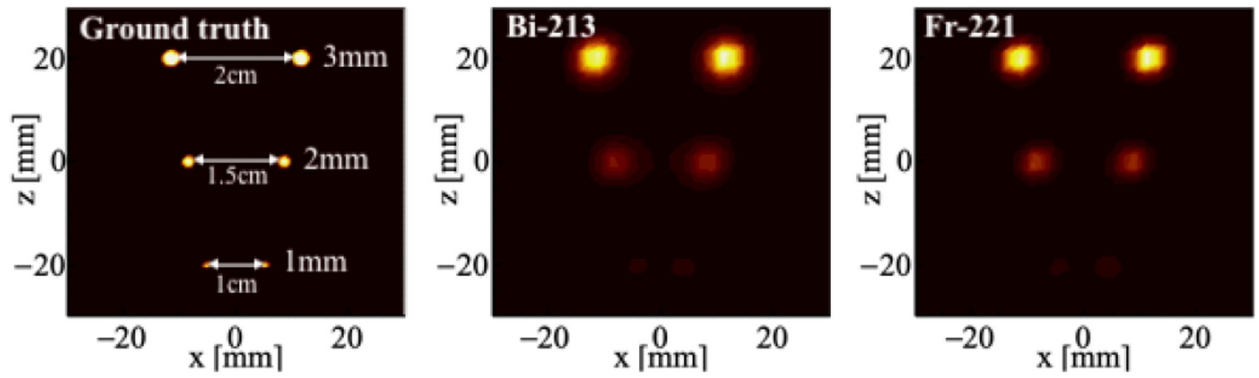
Fig. 11.
Ground truth and proximity-reconstructed images of our custom phantom designed specifically to evaluate proximity imaging. The phantom's activity corresponds to 0.1 μCi of ^{225}Ac and the exposure is 15 minutes. The phantom is located 1 mm from the top scatterer's front face. For these images we use 2.0 mm voxels, 30 subsets and 1 iteration.
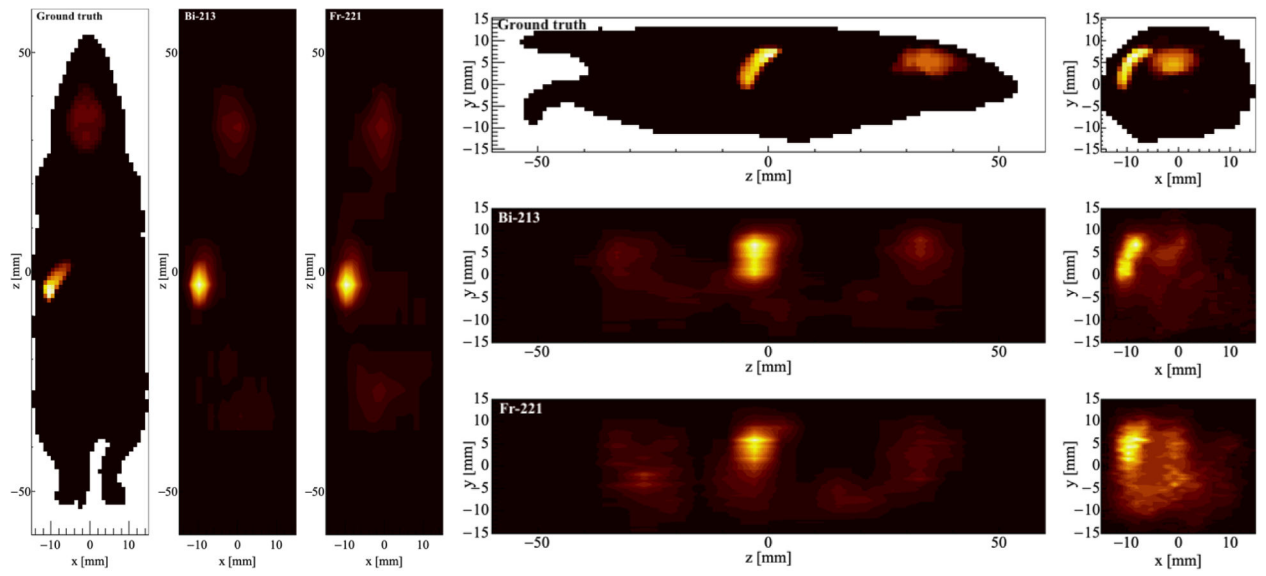
Fig. 12.
Projections of the ground truth and Compton-reconstructed images of a simulated mouse phantom with 0.5 μCi of ^{225}Ac and an exposure of 15 minutes. For these images we use 1.5 mm voxels, 10 subsets and 10 iterations.
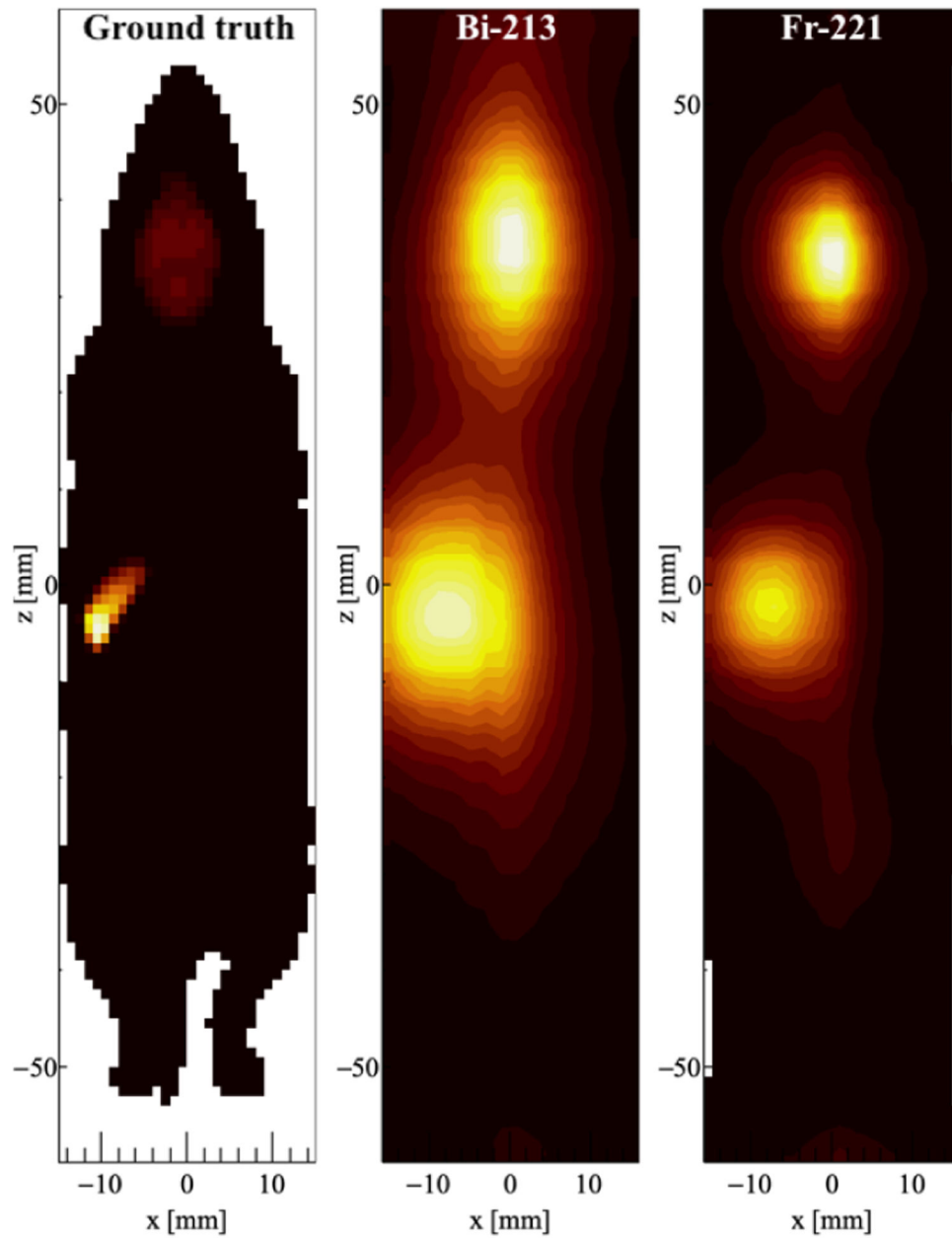
Fig. 13.
Projections of the ground truth and proximity-reconstructed images for a simulated mouse phantom with 0.5 μCi of ^{225}Ac and an exposure of 5 minutes. For these images we use 2 mm × 15 mm × 3 mm voxels in a voxel space of 30×2×40, 30 subsets, and 1 iteration for ^{213}Bi and 5 for ^{221}Fr.
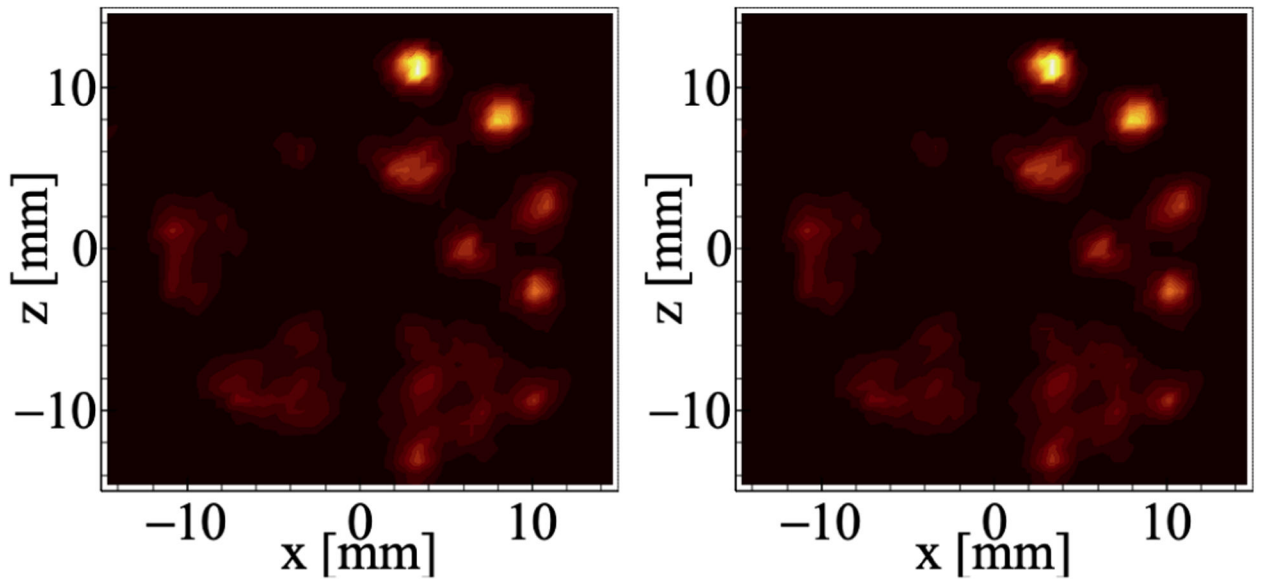
Fig. 14.
Derenzo phantom images obtained by ignoring low activity voxels (left) and using all the voxels (right).

TABLE I

Detector parameters chosen to model our system, and optimal reconstruction parameters.

Parameter	Detector model value	
CZT size	100 mm × 100 mm	
CZT thickness	6 mm	
Scat.-Abs. distance	25 mm	
Pixel size	1 mm	
DOI	1 mm FWHM	
Energy resolution	6.5% FWHM @122keV	
	4.9% FWHM @218keV	
	3.4% FWHM @440keV	
	Compton reco.	**Proximity reco.**
Voxel size	1.5 mm	2 mm
# subsets	10	10
# iterations	10	10